Journal of Volcanology and Geothermal Research 292 (2015) 41–55

Contents lists available at ScienceDirect

Journal of Volcanology and Geothermal Research

journal homepage: www.elsevier.com/locate/jvolgeores

Dynamics within geyser conduits, and sensitivity to environmental perturbations: Insights from a periodic geyser in the El Tatio geyser field, Atacama Desert, Chile

Carolina Munoz-Saez [a,*], Michael Manga [a], Shaul Hurwitz [b], Maxwell L. Rudolph [c], Atsuko Namiki [d], Chi-Yuen Wang [a]

[a] University of California, Berkeley, CA, USA
[b] US Geological Survey, Menlo Park, CA, USA
[c] Portland State University, Portland, OR, USA
[d] Hiroshima University, Hiroshima, Japan

ARTICLE INFO

Article history:
Received 28 September 2014
Accepted 15 January 2015
Available online 24 January 2015

Keywords:
Geysers
Eruptions
Geothermal systems
Bubble trap
Conduit
Choked flow

ABSTRACT

Despite more than 200 years of scientific study, the internal dynamics of geyser systems remain poorly characterized. As a consequence, there remain fundamental questions about what processes initiate and terminate eruptions, and where eruptions begin. Over a one-week period in October 2012, we collected down-hole measurements of pressure and temperature in the conduit of an exceptionally regular geyser (132 s/cycle) located in the Chilean desert. We identified four stages in the geyser cycle: (1) recharge of water into the conduit after an eruption, driven by the pressure difference between water in the conduit and in a deeper reservoir; (2) a pre-eruptive stage that follows the recharge and is dominated by addition of steam from below; (3) the eruption, which occurs by rapid boiling of a large mass of water at the top of the water column, and decompression that propagates boiling conditions downward; and (4) a relaxation stage during which pressure and temperature decrease until conditions preceding the recharge stage are restored. Eruptions are triggered by the episodic addition of steam coming from depth, suggesting that the dynamics of the eruptions are dominated by geometrical and thermodynamic complexities in the conduit and reservoir. Further evidence favoring the dominance of internal processes in controlling periodicity is also provided by the absence of responses of the geyser to environmental perturbations (air pressure, temperature and probably also Earth tides).

1. Introduction

Geysers are springs that produce discrete eruptions of steam, liquid water, and non-condensable gases. Their eruptions are smaller and typically more frequent than volcanoes and hydrothermal eruptions, providing a natural laboratory to study eruptive processes (Kieffer, 1984). Geysers are uncommon; less than 1000 have been described worldwide, and this number is decreasing due to geothermal energy development (Bryan, 1995). Special conditions are needed for their formation: a supply of water, a source of heat, and a particular system of fractures and/or porous rocks to permit episodic discharge (e.g., White, 1967; Fournier, 1969; Kieffer, 1989; Ingebritsen and Rojstaczer, 1993, 1996; Kedar et al., 1998; Kiryukhin et al., 2012; Belousov et al., 2013; Karlstrom et al., 2013; Shteinberg et al., 2013; Vandemeulebrouck et al., 2013; Namiki et al., 2014; Vandemeulebrouck et al., 2014).

There are several open questions about processes and conditions before, during and after the eruption: how is heat transported to and within the geyser system? Do eruptions begin in a conduit as observed in some laboratory experiments (Adelstein et al., 2014)?, or in a deeper reservoir as proposed from limited observations in natural systems (Belousov et al., 2013; Vandemeulebrouck et al., 2013) and experiments (Steinberg et al., 1982)? What is the geometry of subsurface fractures and how do they affect the eruption process? Previous studies of natural geysers provide at least partial answers to these questions. Some observations indicate that prior to an eruption, temperature in the water column is below boiling, and the boiling is caused by ascent-driven decompression (e.g., Bunsen, 1847, Fukutomi, 1942a,b; Kieffer, 1984). Conversely, some studies in Yellowstone National Park (USA) suggested that intermittent injection of superheated water leads to eruption (Rinehart, 1972, 1980), assuming hydrostatic conditions and that the depth of the measurements (23 m) was accurate. White (1967) proposed that eruptions begin with the discharge of water below the boiling temperature (T_{boil}), progress to a liquid-dominated fountain that becomes steam-rich, and end with a quiescent phase. Seismic observations suggest that steam bubbles are crucial in transferring heat to water in the conduit and in driving the eruption (Kieffer, 1984, 1989). Underground cavities at some geysers may create a "bubble trap" that allows

* Corresponding author.
E-mail address: carolimunoz@berkeley.edu (C. Munoz-Saez).

http://dx.doi.org/10.1016/j.jvolgeores.2015.01.002
0377-0273/

for the accumulation of a two-phase fluid (liquid + steam) in the system and the episodic release of this fluid (Mackenzie, 1811; Belousov et al., 2013; Vandemeulebrouck et al., 2013, 2014; Adelstein et al., 2014).

The response of geyser eruptions to external influences provides additional insight into how they work. Some geysers in Yellowstone respond to local and remote earthquakes (Marler, 1964; Rinehart and Murphy, 1969; Marler and White, 1975; Hutchinson, 1985; Husen et al., 2004a,b; Manga and Brodsky, 2006; Hurwitz et al., 2014). The responses of geysers to non-seismic strain (Earth tides, barometric pressure), and weather (atmospheric temperature, rainfall and wind) vary between geysers (e.g., Rinehart, 1972; White and Marler, 1972; Rojstaczer et al., 2003; Hurwitz et al., 2008, 2012, 2014).

Most data used to study geysers comes from observations made at the surface. Data on processes in the ground subsurface of geysers are limited due to the complexity of taking measurements in situ. Active and passive field experiments inside conduits have been performed at Yellowstone National Park (Birch and Kennedy, 1972; Rinehart, 1972; Hutchinson et al., 1997; Kedar et al., 1998), and Kamchatka (Belousov et al., 2013; Shteinberg et al., 2013). Data from these experiments provided a better understanding of conduit geometry (Hutchinson et al., 1997; Belousov et al., 2013), thermodynamic conditions (Hutchinson et al., 1997; Kedar et al., 1998), and recharge processes (Shteinberg et al., 2013).

We obtained continuous time series of pressure and temperature inside the conduit of a geyser located in El Tatio, northern Chile (Fig. 1a). This geyser does not have an official name, so we nicknamed it "El Jefe" (Fig. 1b,c) and use this name throughout the manuscript. This geyser corresponds to feature T35 described in Glennon and Pfaff (2003) as one of the more significant and periodic geysers in the basin. One unusual aspect of the El Tatio geysers is that they are located in the middle of a very dry area, the Atacama Desert, in contrast to other geyser fields in the world (Yellowstone National Park, Kamchatka, Iceland, and New Zealand). The marked daily variation in air pressure and temperature, very high evaporation rates, and the limited meteoric water recharge, make El Tatio's geysers ideal for examining the sensitivity of multiphase systems to external perturbations. A better understanding of "cause and effect" relationship between external conditions and geyser cycle may help to constrain and quantify the processes governing the eruptions.

Down-hole measurements of pressure and temperature from 3531 eruptions of El Jefe geyser during one week in October 2012 provide an extensive record of thermodynamic conditions during the entire geyser cycle. We combined these data with measurements at the surface to: 1) examine the geyser's response to environmental forcing, and; 2) better understand the thermodynamics within the geyser conduit.

We begin with a description of the study area. Then, we describe the field measurements and instruments, followed by a compilation of observations and results. We end with an interpretation of the measurements and evaluate proposed hypotheses for the mechanisms leading to geyser eruptions.

2. El Tatio geyser field

The El Tatio geyser field contains more than 80 active geysers (Glennon and Pfaff, 2003). It is located in northern Chile at an elevation of 4200 to 4300 m. The field is situated among Holocene andesitic stratovolcanoes, which provide the heat for the geothermal system, but no historical eruptions were documented (Lahsen, 1976a,b). Thermal manifestations develop in the hanging wall of a NS trending half-graben (Fig. 1a), that is filled with ~1000 m of sub-horizontal ignimbrites, tuffs and lavas, and covered by Holocene alluvial and glacial deposits (Healy, 1974; Lahsen and Trujillo, 1975). According to the distribution of the geothermal features, the field is divided into a Lower, Middle and Upper Basin (Glennon and Pfaff, 2003) (Fig. 1a). Data from geothermal wells suggest that the permeability is dominated by open fractures in the ignimbrite layers (Cusicanqui et al., 1975, 1976). The maximum temperature measured at the bottom of a 600 m deep geothermal well was 253 °C (Lahsen and Trujillo, 1976).

At El Tatio in October 2012, we measured the average daily air temperature and pressure, which vary between approximately −5 °C to 20 °C and 6.07×10^4 to 6.10×10^4 Pa, respectively. The boiling temperature (T_{boil}) of pure water at these air pressures ranges between 86.2 and 86.4

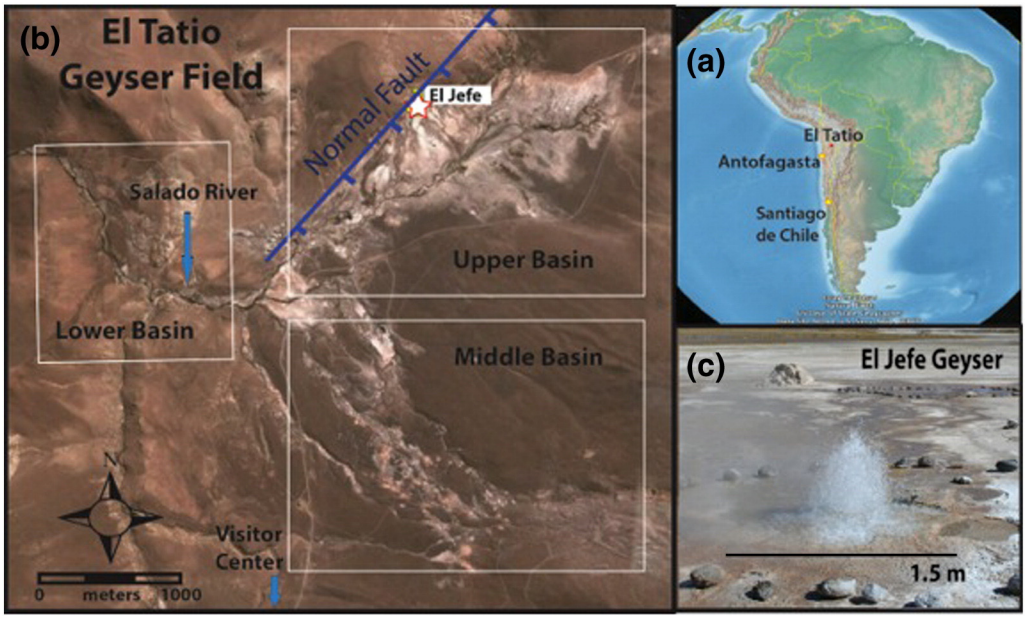

Fig. 1. El Tatio geyser field. (a) Map of South America showing the location of El Tatio in Northern Chile. (b) Aerial photograph of El Tatio Geyser Field (GLCF: Earth Science Data Interface); white boxes show the Upper, Middle, and Lower geyser basins. In the upper basin, El Jefe Geyser (UTM coordinates 601768 E; 7530174 S, WGS84, 19S) is marked by the white star. The blue line indicates the normal fault that bounds the El Tatio half-graben. El Jefe geyser is located in the hanging wall of that fault. (c) El Jefe geyser erupting. (For interpretation of the references to color in this figure legend, the reader is referred to the web version of this article.)

°C (http://webbook.nist.gov/chemistry/fluid/). Evaporation is extremely high, leading to rapid silica deposition (Nicolau et al., 2014).

Most water feeding the geyser field is recharged in the Bolivian Altiplano, 15 to 20 km to the east (Cusicanqui et al., 1976; Lahsen, 1976a,b; Giggenbach, 1978; Munoz and Hamza, 1993; Cortecci et al., 2005). Discharged thermal waters in the El Tatio area have a pH of 6 to 8, and a conductivity of ~20 mS/cm. Most discharged waters have high concentrations of Cl^- (6000 to 8000 mg/l), Na^+ (>3500 mg/l), SiO_2 (>220 mg/l), and As^{3-} (>30 mg/l), and low SO^{4-} (<50 mg/l), (e.g., Cusicanqui et al., 1976; Cortecci et al., 2005; Fernandez-Turiel et al., 2005; Landrum et al., 2009; Tassi et al., 2010; Nicolau et al., 2014). Chemical and isotopic characteristics of thermal waters indicate complex mixing between magmatic, meteoric and hydrothermal sources (Cusicanqui et al., 1975; Giggenbach, 1978; Tassi et al., 2005, 2010).

3. Instrumentation and measurements

Between October 20 and 27, 2012, we deployed a set of instruments at the surface and within the conduit of "El Jefe" geyser (Fig. 1 b,c). To synchronize instruments we used a GPS clock (GlobalSat BU-353 USB GPS Receiver) connected to the computer (HP mini 1000) that started the temperature data loggers.

At the surface, we recorded daytime eruptions simultaneously with a video camera (GoPro, ~30 frames per second) and an infrared video camera (FLIR model A320, ~15 frames per second) for 50 min on October 20, 2012. To detect eruptions throughout the experiment, one thermocouple was placed at the geyser "mouth" (top of the geyser conduit at the ground surface) and a second thermocouple was placed 30 cm above the ground surface. Sensors were attached to a rigid steel rod so that they would not move during eruptions. These pre-calibrated type K thermocouples recorded temperature every 1 s and were in contact with water only during the eruption; between eruptions they recorded air temperature. QuadTemp 2000 (MadgeTech) four channel temperature recorders were used to collect all temperature measurements. Air pressure (P_{air}) was measured every 10 min with a barometer (Setra Model 278).

To measure discharge of the erupted water we placed a rectangular wooden flume (length 65 cm, width 15 cm, height 10 cm) in the wide outflow channel of the geyser. Water discharge was calculated by measuring the velocity of floating objects along the flume using a video camera (videos in electronic supplementary material), and water level in the flume with a ruler. We made measurements during 6 consecutive geyser cycles. Image analysis obtained from the videos was used to estimate the average discharge. Visual observations suggested that the flume captured only ~40–60% of erupted water, with the rest of the water flowing from the pool at the surface back into the conduit. We were unable to better quantify the fate of erupted water.

A GoPro video camera in a custom-built waterproof and insulated housing was lowered into the upper part of the conduit (up to ~0.5 m depth) for one complete geyser cycle to obtain visual images of the conduit geometry and the level of the water during the cycle (videos in electronic supplementary material). However, we observed only the upper conduit (depth up to ~0.7 to 0.8 m) because of the diminution of conduit diameter at depth, and lack of light. We were able to introduce a rigid measuring stick 1.52 cm below the surface.

Inside the conduit, we deployed six pre-calibrated type K thermocouples spaced 30 cm apart, between the conduit mouth and the bottom of the accessible conduit at a depth of 1.5 m (Fig. 2). Temperature was measured every 1 s. The error in the temperature measurements specified by the manufacturer is less than 1.1 °C (http://www.omega.com/thermocouples.html). We attached three absolute pressure transducers mounted in watertight housings (Honeywell models 19C050PA4K and 19C030PA4K) to a rigid metal rod and located them adjacent to the three deeper temperature sensors at 0.9 m, 1.2 m and 1.5 m below the surface (Fig. 2). Measurements were collected at a frequency of 100 Hz with a 24-bit Nanometrics Taurus logger. The data logger had an internal GPS clock to synchronize the measurements. The transducers were calibrated in the laboratory under conditions resembling the down-hole pressures and temperatures at El Jefe. We measured the ground deformation using a surface tiltmeter with a calibrated resolution of 0.23 μrad/mV (Applied Geomechanics Inc. Surface Mount Tiltmeter Model No. 701-2), at a frequency of 2 Hz from October 20 to 22, 2012. The tiltmeter was located 5 m to the East of the vent. We removed the long-term fluctuations with periods greater than the geyser cycle by using a high pass filter $>2 \times 10^{-3}$ Hz. We used data only at restricted time periods (October 20th, 22:00–24:00, October 21st 23:00–24:00, October 22nd 00:00–01:00, 04:00–05:00, UTC time) during which the amplitude of noise was relatively small. Even during these short periods the signals were noisy, and we only used data when the maximum tilt within three eruptions was smaller than 10 μrad.

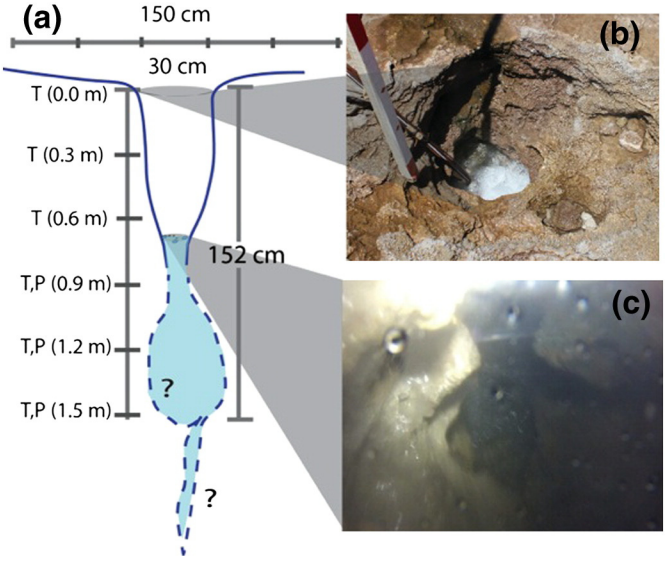

Fig. 2. (a) Illustration of the conduit and the locations of the deployed temperature (T) and pressure (P) sensors. (b) Photograph of the conduit mouth, while the water level was decreasing, showing the string of sensors; distance between the red marks is 30 cm. (c) Photograph of the conduit at the air–water interface (0.6 m) showing the irregular conduit, with constrictions and cracks that intersect the conduit. (For interpretation of the references to color in this figure legend, the reader is referred to the web version of this article.)

4. Data analysis and results

4.1. Pressure and temperature time series and the interval between eruptions (IBE)

The evolution of both pressure and temperature in the conduit is very repeatable between eruptions (Fig. 3a). We calculated the interval between eruptions (IBE) for every geyser cycle using pressure and temperature measurements. To understand the temporal evolution of a single cycle, we compare time series and video observations of the fountain at the surface. We established seven reference points in time (Fig. 3a; green stars numbered 1 to 7), which identify different key stages in the eruption.

(1) Point 1 indicates the beginning of the geyser cycle; it is coincident with the minimum water pressure inside the conduit. After this point, pressure increases while the conduit refills.
(2) Point 2 shows the beginning of a rapid pressure increase, before an eruption.
(3) Point 3 indicates a sudden increase in pressure and temperature. The beginning of fountaining occurs between points 3 and 4.

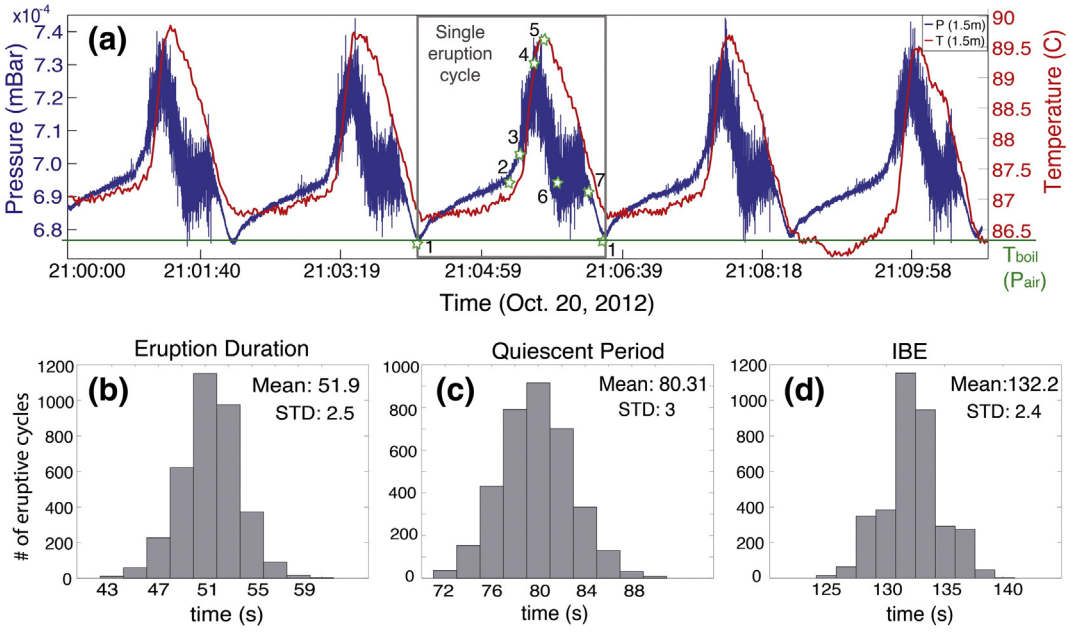

Fig. 3. a) Pressure and temperature time series for a subset of five eruption cycles, at a depth of 1.5 m, on October 20th, 2012. Temperature (red) and pressure (blue) data are plotted on the y-axis, while time is on the x-axis. The box highlights a single cycle. Stars labeled from 1 to 7 identify key stages in the cycle. The green line shows mean boiling temperature (T_{boil} ~86.4 °C) at average local atmospheric pressure. Lower panel shows histograms of the duration of stages of the eruption cycles: (b) eruption duration (points 3 to 7), (c) quiescent period (including relaxation stage, recharge, and pre-eruptive stage, points 7 to 3), and (d) interval between eruptions (IBE). (For interpretation of the references to color in this figure legend, the reader is referred to the web version of this article.)

(4) Point 4 indicates the maximum pressure in the conduit; after this point, pressure decreases at an approximately constant rate.
(5) Point 5 indicates the maximum water temperature; after this point, temperature decreases at an approximately constant rate.
(6) At Point 6 the rate of pressure decrease changes, and corresponds to the end of fountaining at the surface.
(7) Point 7 identifies an increase in the rate of pressure decrease, and the end of the geyser cycle.

During the week of measurements, the mean interval between the 3531 eruptions (IBE) was 132.2 ± 2.4 s (Fig. 3b–d): the eruption itself (points 3 to 7) lasted 51.9 ± 2.5 s, and the quiescent period (including the time from points 1 to 3 and from 7 to 1) was 80.3 ± 3.0 s. Uncertainties shown here and elsewhere are one standard deviation.

In the next sections, we summarize the observations, beginning at the surface and moving progressively downward in the conduit.

4.2. Surface measurements

4.2.1. Geometry of the conduit

The sinter-lined conduit is located in the center of a small depression. The diameter of the conduit opening at the surface is 0.25 m to 0.30 m (the geyser's "mouth" — Fig. 2b). The conduit remains approximately cylindrical to a depth of 0.8 m, below which it narrows. Because we could insert a metal rod to depths of 1.52 m, at greater depth the conduit either has a constriction with a diameter less than ~2 cm, or it bends (Fig. 2). Fissures and other cavities of unknown dimensions intersect the conduit (Fig. 2c). Video observations inside the conduit suggest that during the quiescent period the conduit is partially full of water with the minimum water level (air–water interface) at ~0.75 to 0.80 m of depth. The depth of air–water interface varied during the geyser cycle; it increases by ~0.25 m during the quiescent period.

4.2.2. Environmental perturbations

Fig. 4 shows the power spectra for water pressure and temperature inside the geyser, air temperature and pressure, and Earth tides. At high frequencies we recognized a strong and sharp peak in water pressure and temperature, which corresponds to the IBE (Fig. 4a). At lower frequencies we identify the daily signals of barometric pressure, atmospheric temperature and tides. The phase and amplitude of solid Earth tides were calculated theoretically using the SPOTL software package (Agnew, 2012).

4.2.3. Temperature measurements above the ground surface

We overlapped the time series of temperature above the ground surface (for 2 eruptions) with the infrared video (FLIR) recording. We observed the eruptions of hot water at the surface for only ~35 s (Fig. 5, points 3 to 6), while at depth the water stays hot for longer (Fig. 5, points 3 to 7). The maximum water ejection height (2 m) observed in the FLIR images coincided with the highest temperature measured by the thermocouple at the ground surface (~83 °C), which remained almost constant during the eruption, a few degrees below T_{boil}, due to cooling in the atmosphere (Fig. 5, points 4 to 5). At the end of the eruption (Fig. 5, between points 5 and 6), the temperature at the surface sensor decreased rapidly, recording air temperature.

4.2.4. Discharge measurements

From discharge measurements we obtained an average volumetric flow rate of 1.9×10^{-3} m^3/s during the eruption, corresponding to a mass flow rate of 1.8 kg/s (using a hot water density of 970 kg/m^3). The water flowed through the flume for ~35 s (the duration of eruptions at the surface). The measured discharge is a lower bound on the erupted volume since we estimated visually that 40–60% of the water flows back into the geyser rather than flowing through the flume. There are holes in the ground close to the vent that also drained water back to the conduit (videos in electronic supplementary material). The volume measured flowing through the flume is still probably representative of the average net mass discharge from the system. Given the calculated mass flow rate, the net erupted mass is 66 kg. As this value is perhaps <60% of the total amount of water erupted, we expect that total mass erupted is >110 kg per cycle. The mean net mass flow rate for a geyser cycle is 0.83 kg/s (total erupted mass divided by IBE).

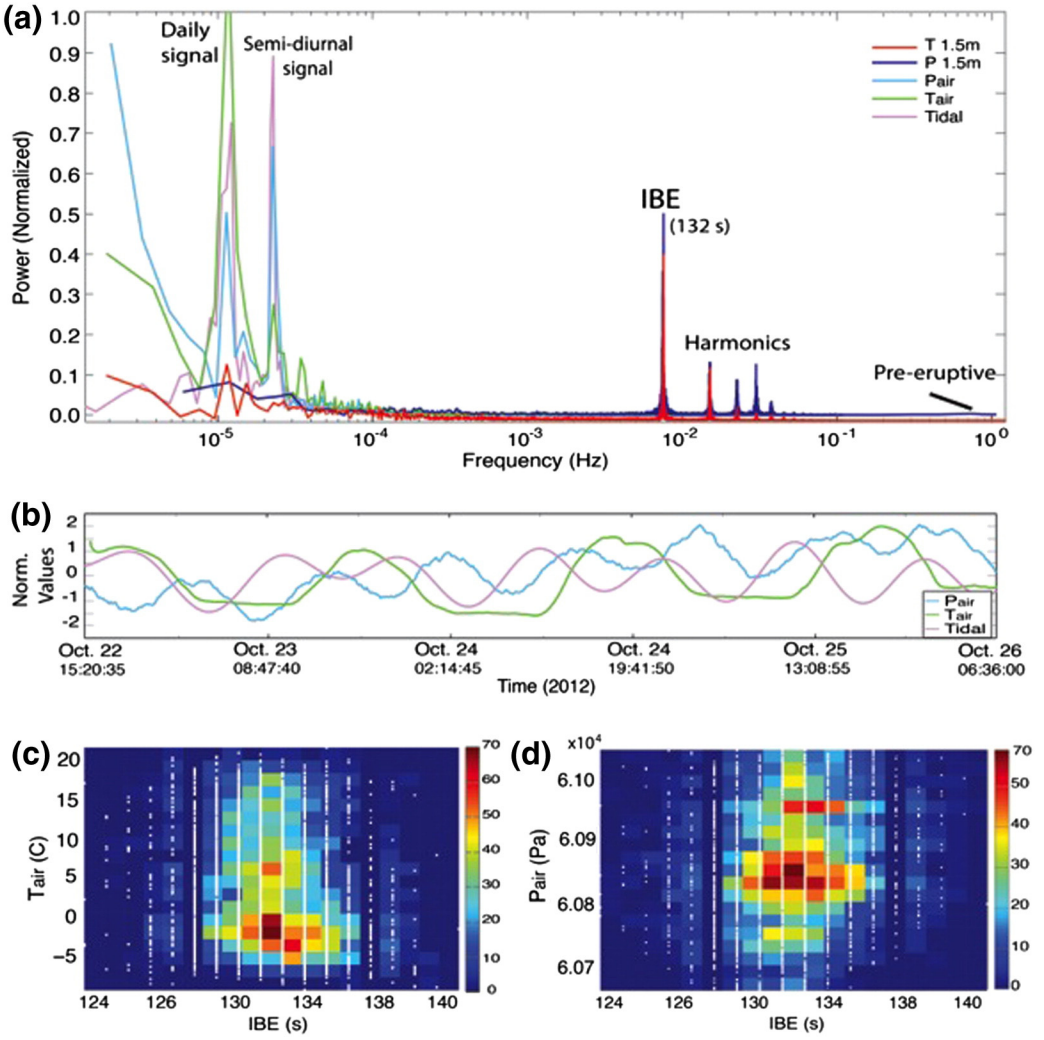

Fig. 4. (a) Power spectra of pressure (blue) and temperature (red) inside the geyser (1.5 m), and external periodic daily signals: air temperature (T_{air}), atmospheric pressure (P_{air}), and calculated solid Earth tides (Tidal). Values on the y-axis were normalized to have the same scale. One day period observed in the water temperature (1.5 m) data is an instrumental artifact and not a real signal. (b) Time series for 3.5 days showing daily variations of air temperature, atmospheric pressure and solid Earth tides. Values shown on y-axis were normalized ((Value − mean(Value)) / Std(Value)). (c) and (d) are 2-D histograms: white dots show the data, and colors show number of dots plotting in that region (color bar). (c) IBE as a function of air temperature, the coefficient of correlation is $r^2 = 0.01$ (d) IBE as a function of atmospheric pressure, the coefficient of correlation is $r^2 = 0.02$. (For interpretation of the references to color in this figure legend, the reader is referred to the web version of this article.)

4.2.5. Ground deformation

Fig. 6a shows water pressure in the conduit, and Fig. 6b and c show the corresponding tilt of the ground surface. We stacked tilt data of ~130 eruptions and calculated the average shown by black curves in Fig. 6b and c. Both tilt vectors indicate that eruptions produce measurable ground deformation. Fig. 6b shows a small tilt increase during the resting time and a large increase during the eruption, followed by a decrease at the end of eruption. Fig. 6c for the tangential direction shows an increase of the tilt during the quiescent time; but it does not show a signal at the beginning of the eruption. We cannot exclude the possibility that the temporal tilt pattern could be a result of water ponding in the pool during the eruption rather than subsurface sources of pressure changes.

4.3. Measurements in the conduit

Because the temperature and pressure waveforms of all the eruptions are very similar (Figs. 2 and 3), we stacked the waveforms of all 3531 eruptions and calculated the average value of temperature and pressure throughout an "average" eruption (Figs. 7 and 8).

We define the upper conduit as the part of the conduit without water during quiescent period, from the surface to the air–water interface right before an eruption (~0.6 m from surface). Once water at the air–water interface reaches T_{boil} (Fig. 7c, points 3 to 4) the eruption starts, and boiling water moves rapidly upward through the conduit, reaching the upper sensors in the conduit (Fig. 7ab, points 3 to 4), and the surface (Fig. 5, points 3 to 4). After the ~35 second duration of the eruption (Fig. 7ab points 3 to 5), temperature decreases continuously as the water level decreases.

The temperature at the top of the water column remains constant at T_{boil} for ~45 s (Fig. 7c, points 3 to 7). Subsequently, the temperature drops ~15 °C as cooled erupted water from the surface, and air enter into the conduit (Fig. 7c, points 7 to 1, video in electronic supplementary material). The high concentration of dissolved ions in the water does not increase the boiling temperature significantly (<0.15 °C for concentrations of 8 g/l of NaCl dissolved in water).

We define the lower conduit as the part of the conduit below the air–water interface before the eruption, to a depth of 1.52 m. We observe that before the eruption (points 1 to 3), the temperature of the water is almost constant at all depths, close to T_{boil}. Temperature in the lower conduit then increases (Fig. 8, from points 3 to 5) once the geyser

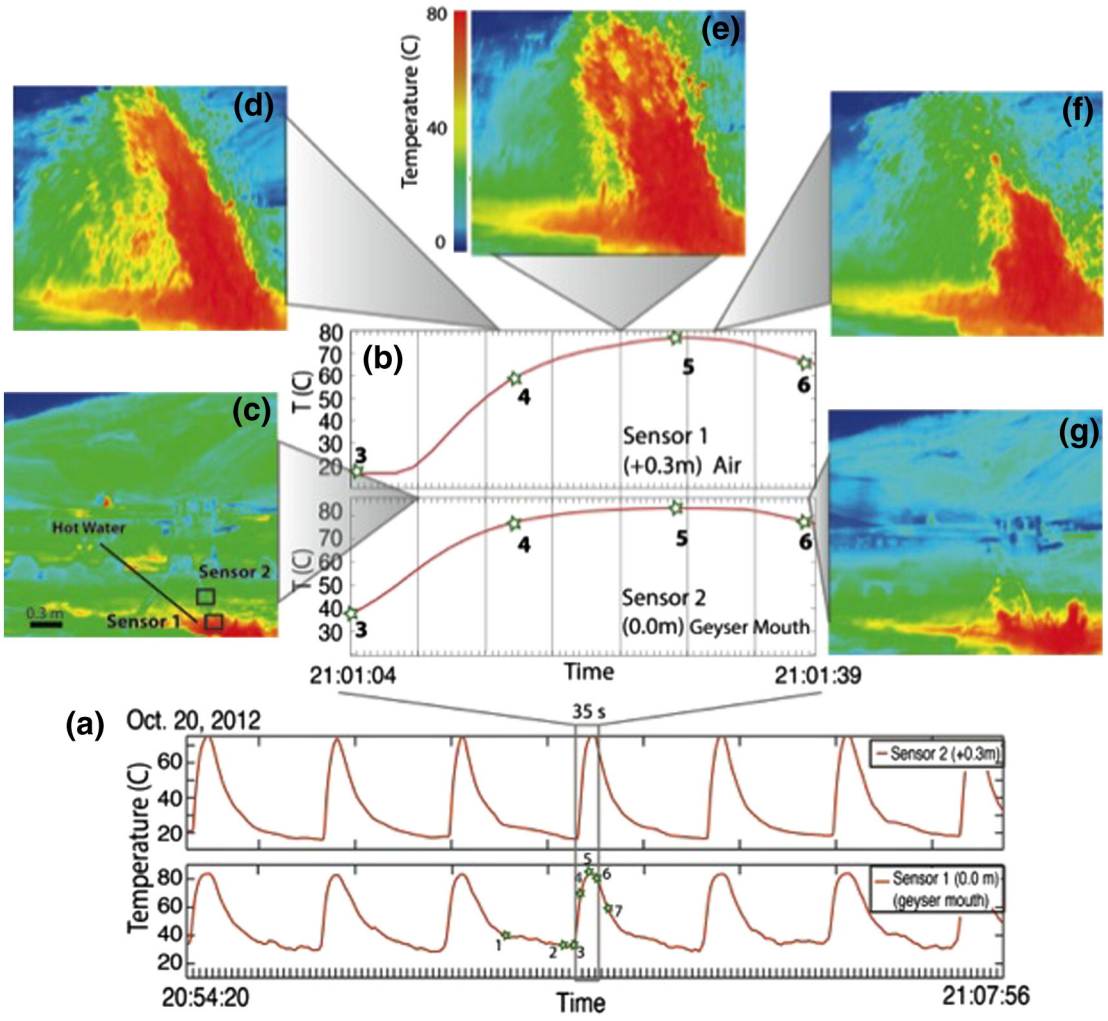

Fig. 5. (a) A sub-sample of the temperature time series for two sensors at the surface. Every peak represents an eruption. Sensor 1 is located at the geyser mouth. Sensor 2 is located 0.3 m above the conduit mouth. Sensors were in the air before eruptions occur. During the eruption, temperature increased because hot erupted water reached the sensors. (b) Zoom on 35 s of a single eruption (box). Stars with numbers are the key stages in the eruption cycle defined in Fig. 3, but for a different eruption. Images (c) to (g) were taken with a FLIR camera (extracted from the video every ~6 s) during the same eruption. High temperature, in red, is related to boiling water coming out of the conduit during the eruption. Image (c) was taken shortly after the start of the eruption at point 3, and it shows the high temperature in the mouth of the conduit. Between points 4 and 6, temperature remains close to T_{boil}, the boiling point; subsequent images (d), (e), and (f) show a high volume of hot water coming out of the conduit. At point 6, temperature decreases (sensor in contact with air). The volume of hot water drops (image (g)) identifying the end of the eruption at the surface. (For interpretation of the references to color in this figure legend, the reader is referred to the web version of this article.)

is erupting at the surface (Figs. 5 and 7). Pressures at depths of 0.9 m and 1.2 m reach maximum values (Fig. 8ab) during the first half of the surface eruption (Figs. 5 and 7, from points 3 to 4). However, at a depth of 1.5 m, pressure between points 3 to 4 is almost constant, with a slightly noticeable maximum between these points. Temperature increases 3 ± 1 °C. The very small change in pressure, and comparably larger change in temperature between points 3 and 4, suggests that heat is added, but with little additional mass.

Pressure decreases from points 4 to 7 (Fig. 8abc), and temperature continues to increase until point 5. Water at a depth of 0.9 m reaches boiling conditions at point 5 (Fig. 8a). Small changes in temperature and a large decrease in pressure around point 5 are consistent with adiabatic decompression of water in the conduit. Water at the deepest sensors reaches boiling conditions close to point 6 (Fig. 8bc), suggesting a downward propagation of the boiling front into the conduit (Figs. 5, 7, and 8). At a depth of 0.9 m, boiling conditions (Fig. 8a, points 5 to 7) are maintained beyond the end of the eruption at the surface (Figs. 5 and 7, point 6).

Fig. 8 shows that from points 6 to 7, changes in pressure are small; the pressures at 0.9 m and 1.2 m decrease slightly but at a depth of 1.5 m pressure increases slightly. The temperature shows a marked decrease of about 1 °C at all sensors, suggesting heat loss or exchange with cooler water. After that, pressure and temperature from points 7 to 1 decrease and remain close to the boiling curve until the system returns to the initial conditions (close to T_{boil}).

Fluctuations in pressure from points 3 to 7 (Figs. 3, 6, and 8) are coincident with T_{boil} at a depth of 0.6 m (Fig. 7c). Considering the uncertainties in the temperature, there is no clear evidence of superheated fluid; if superheated fluid is present (points that are to the right of the boiling curve in Fig. 8), superheating is not sustained in time.

5. Discussion

5.1. Modulation of the IBE

An important observation made at El Jefe was the consistent timing and evolution of the eruptions (at least within the week of measurements) despite the fact that a large amount of the erupted water cools at the surface and recharges the geyser system. Lengthening of geyser IBE, as a result of decreases in the air temperature, has been reported in pool geysers (Merzhanov et al., 1990; Hurwitz et al., 2014). This lengthening occurs because the large surface area of pool geysers

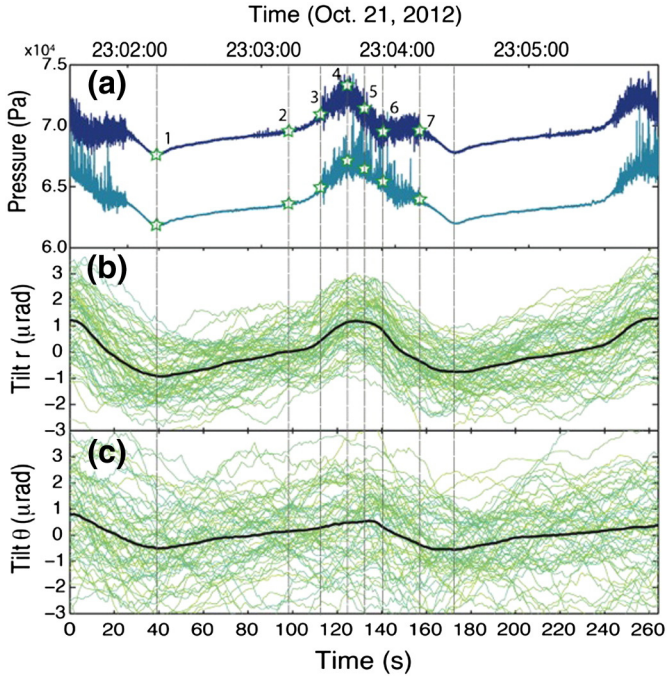

Fig. 6. (a) The pressure measured at depths of 1.5 m (dark blue) and 0.9 m (light blue). (b) and (c) show the ground deformation recorded by a tiltmeter, in the radial and tangential directions, respectively. A positive sign indicates that the ground rises in the direction of vent and to the north, respectively. Black curves are the averaged signals. Yellowish to bluish curves are for individual eruptions. (For interpretation of the references to color in this figure legend, the reader is referred to the web version of this article.)

enhances heat loss to the surroundings; thus, IBE increases as air temperature decreases and wind speed increases (Hurwitz et al., 2014). The extremely regular IBE and very weak correlation between the IBE and air temperature ($r^2 = 0.01$) suggest that there is no significant influence of air temperature on the geyser cycle. The constant value of IBE also implies that large variations in wind speed and hence evaporation (which we did not measure) may have negligible influence.

Stresses induced by barometric pressure changes (3×10^2 Pa) and solid Earth tides (10^3 Pa) can potentially produce poroelastic perturbations in the conduit and/or reservoir that interfere with bubble nucleation and growth, or change permeability, hence changing the time to reach critical conditions for an eruption (Hutchinson et al., 1997; Vandemeulebrouck et al., 2013). Although one week of data may not be enough to establish a clear correlation, El Jefe Geyser does not show variation of the IBE related to external stress changes, consistent with measurements at geysers in Yellowstone (White and Marler, 1972; Rojstaczer et al., 2003; Hurwitz et al., 2014). Pressure perturbations greater than 3×10^2 Pa may thus be required to affect the IBE of El Jefe.

The regularity of El Jefe's IBE and the weak modulation of its IBE by external conditions suggest that the behavior of some geysers is dominated by internal processes (Bloss and Barth, 1949; Marler, 1951; Rojstaczer et al., 2003; Hurwitz et al., 2014). The geometry and thermodynamic state of the reservoir and/or deeper conduit must dominate the periodicity of El Jefe geyser. The insensitivity to changes in ambient temperature implies that the erupted volume is smaller than the subsurface reservoir, or the amount of cooled water that flows back into the conduit is not significant compared with hotter water coming from below.

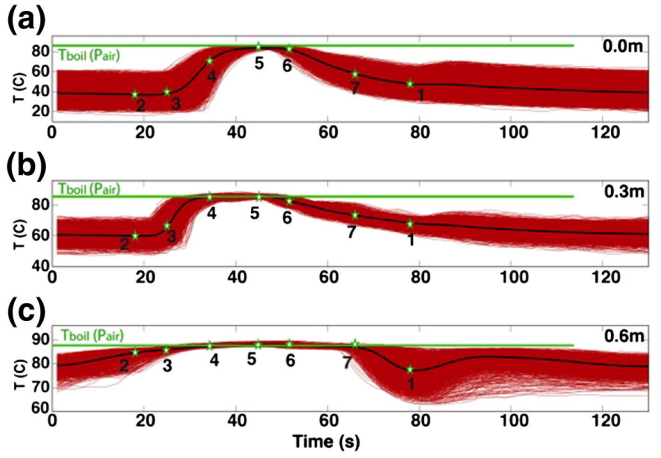

Fig. 7. Temperature in the shallowest part of the conduit for 3531 geyser cycles at depths of (a) 0.0 m, (b) 0.3 m, and (c) 0.6 m. The geyser cycles (red curves) are stacked and averaged (black curves). Range of time is the IBE (132 s). The green line shows the boiling temperature (T_{boil}) for the corresponding air pressure (P_{air}). From points 2 to 3, the temperature increases. After point 3, water reaches the boiling curve at 0.6 m, and the eruption starts. Between points 4 and 5, boiling water reaches the shallowest sensors at 0.3 m and 0.0 m. Between points 6 and 7, water continues to boil at 0.6 m, but boiling water does not reach the shallowest sensors and the eruption ends at the surface. At point 1, cooled erupted water returns to the conduit and the cycle starts again. (For interpretation of the references to color in this figure legend, the reader is referred to the web version of this article.)

5.2. Duration of the eruption and the quiescent period

Steinberg et al. (1982) and Shteinberg (1999) developed a model to explain a relationship between the quiescent period and the duration of the previous eruption in which heat and water are provided by two sources: a cold reservoir with recharge controlled by pressure in the conduit, and a hot reservoir with a constant recharge to the system. A longer eruption would remove more heat and mass from the system, and thus the time needed for the next eruption would increase. In contrast, IBE shows no real variation, and we observed that the duration of an eruption and its subsequent quiescent period has a weak negative relationship (Fig. 9, a), though the correlation coefficient is small and the distribution is nearly uniform (Fig. 3b–d). The length of quiescent period before the eruption and the IBE are unrelated with the eruption duration (Fig. 9: b, c). Temperature data do not indicate that accumulating heat is transferred to the near-surface conduit during the quiescent period, but rather, temperature is almost constant, suggesting that a single reservoir dominates recharge to the conduit. The addition of heat occurs at the end of recharge, which we attribute to steam coming from below over a short time interval, not at a constant rate.

5.3. Eruption stages

We apply idealized models to interpret pressure and temperature measurements, with the objective of constraining or inferring key processes and properties: the recharge from the reservoir into the conduit; hydrogeologic parameters of the conduit; steam mass fraction before and during the eruption; sound speed; and the possibility of choked flow at the vent (Table 1).

Previous authors (e.g., Kieffer, 1984; Karlstrom et al., 2013, Namiki et al., 2014; Adelstein et al., 2014) described a preparation stage preceding major eruptions called "pre-play", which is characterized by pulses of liquid and/or steam discharge. At El Jefe we also document a preparatory phase in the form of the oscillations preceding every eruption, but without surface discharge.

5.3.1. Recharge of the conduit

During the quiescent period, water level changes by ~0.25 m. The equivalent radius of a cylinder with volume >110 l (our estimate of erupted volume) is >0.38 m, greater than the dimensions seen by the

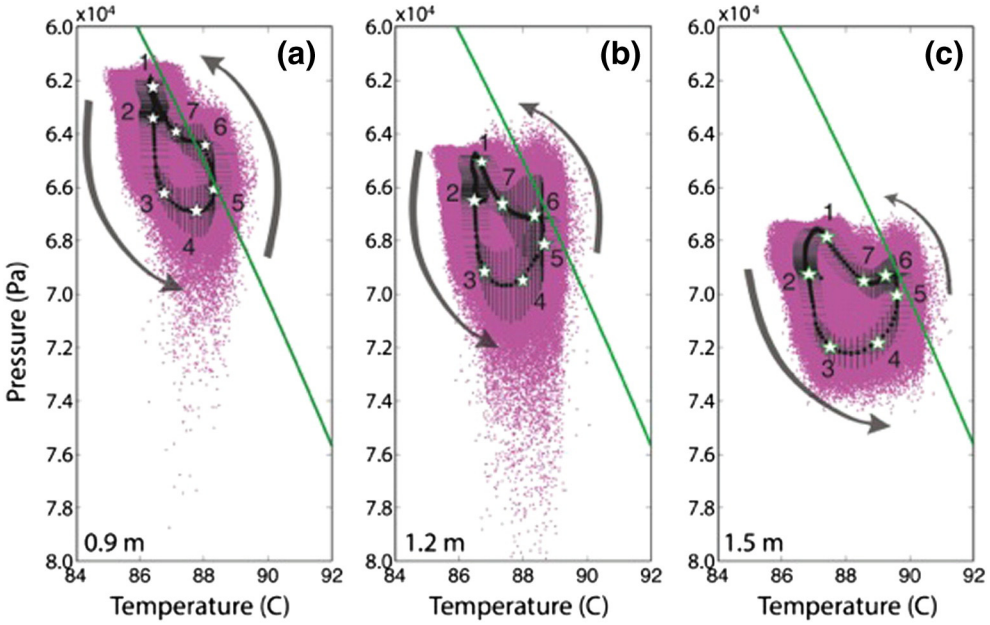

Fig. 8. Water pressure and temperature during the eruption cycles, for ~3531 eruptions. Gray arrows show the evolution of pressure and temperature with respect to time (stars 1 through 7: $t_1 = 0$ s, $t_2 = 65 \pm 2$ s, $t_3 = 70 \pm 2$ s, $t_4 = 85 \pm 2$ s, $t_5 = 100 \pm 2$ s, $t_6 = 105 \pm 2$ s, $t_7 = 120 \pm 2$ s. Black curves show the average and the black bars show the standard deviation of the data. Green lines show the calculated boiling curve for pure water. (For interpretation of the references to color in this figure legend, the reader is referred to the web version of this article.)

video camera ($r < 0.15$ m), implying that cavities and fractures imaged by the video camera that intersect the conduit (Fig. 2) contain water that erupts.

Estimated mean net mass flow of 0.83 kg/s for El Jefe is similar to the estimate of 0.68 kg/s made at Old Faithful Geyser of Calistoga, California, USA (Rudolph et al., 2012). The mass flow rate is smaller than at Lone Star geyser in Yellowstone National Park, 1.9 kg/s (Karlstrom et al., 2013), and Old Faithful, 7.0–8.3 kg/s, using a measured discharge of 38–45 m^3 (Allen and Day, 1935).

We define the beginning of each cycle by the initiation of recharge of the conduit as documented by an increase in pressure (points 1 to 3). The rate of pressure increase decays exponentially during most of the recharge period (Fig. 11d) and it is similar to models and measurements at other geysers (e.g., Steinberg et al., 1982; Kedar et al., 1998; Rudolph et al., 2012; Shteinberg et al., 2013). The water level in the conduit $Z(t)$ increases from the initial value Z_0 owing to the recharge of water. Taking the base of the conduit as a reference, the total water level $Z(t)$ increases (Fig. 10) as

$$Z(t) = Z_c(t) + Z_0. \tag{1}$$

The mass flow rate during the recharge of the conduit $G(t)$, assuming a constant water density (ρ) and a constant cross section of the conduit (S), changes the water level (Fig. 10):

$$G(t) = \rho S \frac{dZ(t)}{dt}. \tag{2}$$

Even though we observe that the conduit width varies with depth, we assume that it is constant to simplify the equations.

Total pressure inside the conduit during the recharge, $P(t)$, can be determined assuming that it is close to hydrostatic conditions, i.e., $P(Z, t) = \rho g Z(t)$, with g being the gravitational acceleration.

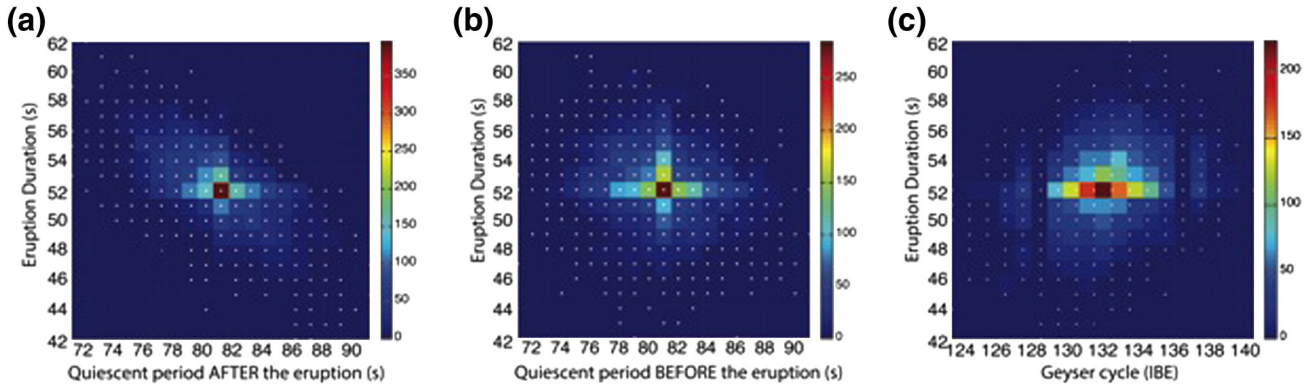

Fig. 9. 2-D histograms of (a) relationship between eruption duration and duration of following quiescent period, the coefficient of correlation is $r^2 = 0.4$; (b) relationship between eruption duration and duration of previous quiescent period, the coefficient of correlation is $r^2 = 0.03$ (c) Relationship between eruption duration and IBE, the coefficient of correlation is $r^2 = 0.06$. IBE is defined for an entire geyser cycle: the period between the beginning of an eruption and the beginning of the next eruption (eruption duration plus the quiescent period after eruption). White dots show the data, and colors show the number of observations plotting in that region (color bar). (For interpretation of the references to color in this figure legend, the reader is referred to the web version of this article.)

Table 1
Summary of parameters.

Parameter	Value	Unit	Description
A	–	m^2	Cross-sectional area of flow of water from the aquifer to the conduit
α	–	m × s	Constant of proportionality between mass flow rate and pressure inside conduit
Cp	–	$\frac{J}{kg\ K}$	Heat capacity of water
f	–	Hz	Frequency of resonance
g	9.8	$\frac{m}{s^2}$	Acceleration of gravity
G_o		$\frac{kg}{s}$	Initial and constant mass flow rate of water coming from hypothesized reservoir or aquifer
$G(t)$	–	$\frac{kg}{s}$	Total mass flow rate of water during the recharge
h	–	m	Height of the eruptive column
$H(t)$	–	$\frac{J}{s}$	Heating rate during the recharge calculated from model
$H_{erupted}$	–	J	Heat needed to generate an eruption
k	–	m^2	Permeability of the conduit
K	–	$\frac{m}{s}$	Hydraulic conductivity
L	–	m	Distance over which water flows from the aquifer to the conduit
m	–	kg	Total mass of water erupted
$M(t)$	–	kg	Mass of water in the conduit during recharge
n	1	–	Fundamental mode of resonance
P_{air}	6.07×10^4 to 6.1×10^4	Pa	Atmospheric pressure measured at El Tatio, 4200 m of elevation
P_0	–	Pa	Initial hydrostatic pressure in the conduit
P_{0_in}	–	Pa	Initial hydrostatic pressure inside of the conduit, below the sensor.
P_{0_sen}	–	Pa	Initial hydrostatic pressure inside of the conduit, above the sensor.
$P(t) = P(Z,t)$	–	Pa	Total hydrostatic pressure
$P_c(t)$		Pa	Hydrostatic pressure above Z_0
$P_{sen}(t)$		Pa	Hydrostatic pressure above the sensor
P_∞	–	Pa	Pressure in the hypothesized reservoir
$Q(t)$	–	$\frac{m^3}{s}$	Volumetric flow rate into the conduit
r	0.15–0.38	m	Radius of the conduit, assuming a cylindrical shape
ρ	~970	$\frac{kg}{m^3}$	Density of water at T_{boil}
S	–	m^2	Cross section area of the conduit with radius r
t	–	s	Time
T_{air}	−5 to 25	°C	Measured atmospheric temperature
T_{boil}	86.2–86.4	°C	Boiling temperature at P_{air}
T_0	–	°C	Initial temperature at the bottom of conduit before recharge
$T(t)$	–	°C	Temperature inside the conduit during the recharge
T_∞	–	°C	Temperature in the hypothesized reservoir or aquifer
U	–	$\frac{m}{s}$	Sound speed of water
v	–	$\frac{m}{s}$	Exit velocity from the conduit to the surface
μ	0.335×10^{-3}	Pa s	Dynamic viscosity of water at T_{boil}
Z_0		m	Initial water level into the conduit at the beginning of the recharge
Z_{0_in}	–	m	Initial water level into the conduit, below the sensor
Z_{0_sen}		m	Initial water level into the conduit, above the sensor
$Z(t)$	–	m	Water level in the conduit during the recharge
$Z_{sen}(t)$	–	m	Water level into the conduit during the recharge, above the sensor
$Z_c(t)$	–	m	Water level into the conduit during the recharge, above the Z_{0_sen}

Following previous approaches (Steinberg et al., 1982; Kedar et al., 1998; Rudolph et al., 2012; Shteinberg et al., 2013), we assume that recharge $G(t)$ into the conduit is linearly proportional to the pressure difference between the reservoir (P_∞) and the conduit (Fig. 9),

$$G(t) = -\alpha\,(P(t) - P_\infty). \tag{3}$$

This expression is analogous to Darcy's law if we neglect pressure diffusion in the system providing the recharge. By analogy to Darcy's law, the constant of proportionality, α, depends on the hydraulic conductivity K, the distance L to the reservoir, and the surface area, A, over which recharge occurs. Here, A is again assumed to be constant, and not dependent on water level. The constant α in Eq. (3) can be related to equivalent quantities in previous models (Steinberg et al., 1982; Kedar et al., 1998; Rudolph et al., 2012):

$$\alpha = \alpha_{\text{Steinberg}} = S\rho/\alpha_{\text{Kedar}} = \alpha_{\text{Rudoph}}/\rho.$$

From Eqs. (2) and (3), we obtain

$$\left(\frac{S}{g}\right)\frac{dP(t)}{dt} = -\alpha\,(P(t) - P_\infty). \tag{4}$$

Integrating, and applying the initial condition P_0 at t = 0

$$P(t) = P_\infty + (P_0 - P_\infty)\left(e^{\frac{-t\alpha g}{S}}\right). \tag{5}$$

The pressure measured at the sensor $P_{sen}(t)$ is related to the total pressure by

$$P_{sen}(t) = P(t) - P_{0\_in} \tag{6}$$

where P_{0_in} is the difference of hydrostatic pressure between the reservoir and the sensor (Fig. 10)

$$P_{sen}(t) = (P_\infty - P_{0\_in}) - (P_\infty - P_0)\left(e^{\frac{-t\alpha g}{S}}\right). \tag{7}$$

Fitting the data from the sensor located at a depth of 1.5 m with Eq. (7), from points 1 to 2, we obtain

$$\left(P_\infty - P_{0_{in}}\right) = 6.97 \times 10^4 \pm 4 \times 10^2 \text{ Pa} \tag{8}$$

$$(P_\infty - P_0) = 2.10 \times 10^3 \pm 2 \times 10^2 \text{ Pa} \tag{9}$$

$$\frac{S}{\alpha g} = 43 \pm 4 \text{ s}. \tag{10}$$

Considering that $P_0 = P_{0\_sen} + P_{0\_in}$, from Eqs (8) and (9) we obtain

$$P_{0\_sen} = 6.76 \times 10^4 \pm 1 \times 10^2 \text{ Pa}. \tag{11}$$

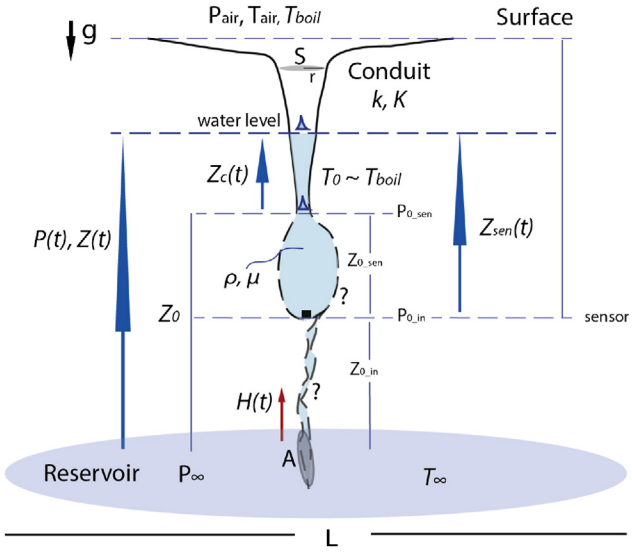

Fig. 10. Schematic illustration of the geyser subsurface showing parameters used in the recharge model.

The reasonable fit between the observed and modeled pressure suggests that recharge is dominated by the water level in the conduit. However, toward the end of recharge (Fig. 11, points 2 to 3), the rate of pressure increase is greater than predicted by the model and deviates from the exponential fit. This misfit may be the result of the decrease in diameter of the upper conduit. Additionally, we calculated the exponential fit between points 2 and 3. Using Eq. (10)and the new fitting (considering the same αg), we infer that the surface area between points 1 and 2 is 4.5 times greater than the surface area between points 2 and 3. By the end of the recharge period, water reaches the upper conduit where the radius was ~0.15 m, whereas the lower conduit radius is estimated to be ~0.32 m. From the total erupted volume, the equivalent radius was estimated to be ~0.38 m. Assuming S for a conduit of constant radius (r ~ 0.38 m) (Fig. 10), from Eq. (10) we calculate

$$\alpha = 3.40 \times 10^{-4}. \tag{12}$$

If we treat the rock around the conduit as a porous medium, the volumetric flow $Q(t)$ is given by

$$Q(t) = -K\frac{A}{L}(Z(t) - Z_0). \tag{13}$$

Then, Eq. (4) is written as

$$Q(t) = -g\alpha(Z(t) - Z_0) \tag{14}$$

$$\alpha = -\frac{K}{g}\left(\frac{A}{L}\right). \tag{15}$$

We can estimate the ratio $\frac{A}{L}$ as a function of permeability, $k = K\mu/\rho g$. If the recharging system has $k > 10^{-9}$ m^2, $\frac{A}{L} < 0.1$ m (using a viscosity of 0.335×10^{-3} Pa s at T_{boil}), which implies a thin and long fracture. If $k < 10^{-11}$ m^2, $\frac{A}{L} > 12$ m, and a much thicker region provides recharge.

Previous models considering two sources of water suggested that hot water from below provide a constant heat input (Steinberg et al., 1982; Kedar et al., 1998). Those models predict an exponential increase of temperature in the conduit during the recharge. To test those models, we consider a constant heat input $H(t)$ of liquid water coming from below with mass flow rate in the conduit $G = \frac{dM(t)}{dt}$, where M is the mass

$$H(t) = C_P\, G(t)\, (T(t) - T_0). \tag{16}$$

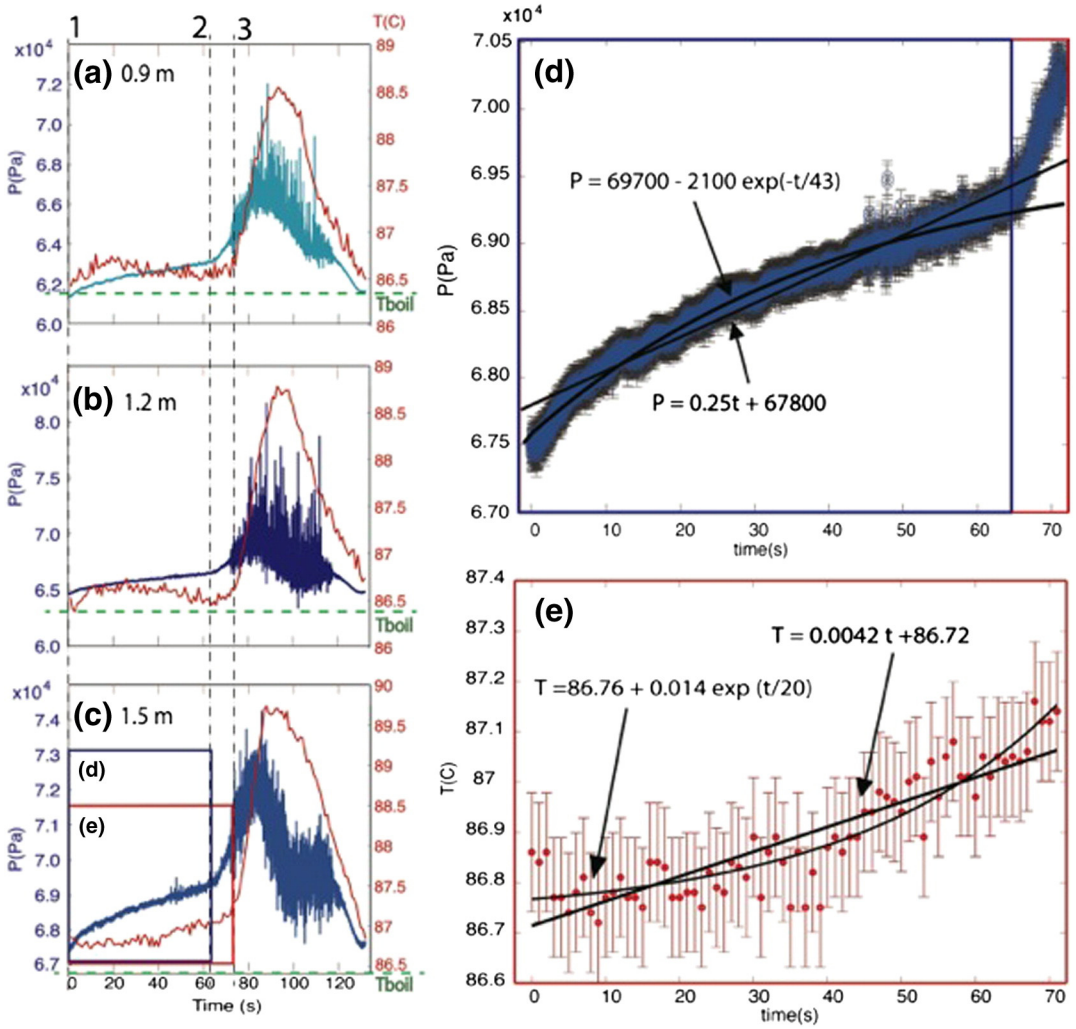

Fig. 11. Data from sensors located at (a) 0.9 m, (b) 1.2 m, and (c) 1.5 m. Pressure (blue) and temperature (red) data on the y-axes, and time for a single eruption cycle on the x-axis. Green line shows the boiling temperature at atmospheric conditions T_{boil} (86.4 °C). Numbers 1, 2 and 3 are the same key points described in previous figures. (d) Shows the pressure during the resting time. Fitting curves of the data are the black lines, and vertical gray lines show ±1 standard deviation. (e) Temperature during the same period. Fitting curves are the black lines, and the red vertical lines show ±1 standard deviation. (For interpretation of the references to color in this figure legend, the reader is referred to the web version of this article.)

If the initial temperature (T_0) is constant

$$T(t) = T_0 + \frac{H(t)}{G(t)\, C_P}. \tag{17}$$

From Eqs. (3) and (7) we obtain the total mass flow $G(t) = G_0\left(e^{\frac{-t\alpha g}{S}}\right)$, and with $H(t) = H$,

$$T(t) = T_0 + \frac{H}{(G_0 C_P)}\, e^{\frac{t\alpha g}{S}}. \tag{18}$$

Fitting an exponential curve to the temperature data (Fig. 11e):

$$\frac{H}{(G_0 C_P)} = 0.014 \pm 0.003^{\circ}\mathrm{C} \tag{19}$$

$$\frac{S}{\alpha g} = 20 \pm 5\ \mathrm{s}. \tag{20}$$

The constant given in Eq. (20) is different from the equivalent one obtained from pressure data in Eq. (10). Temperature at a depth of 1.5 m is nearly constant, and increases only toward the end of the recharge period (Fig. 11c). It is this increase that drives the fit in Eq. (18). We propose next that the discrepancy between the two values implies that heat input is not constant, and that there is an additional source of heat provided by steam during the later stages of recharge.

5.3.2. Pre-eruptive pressure signal

The pressure difference between the sensors at 0.9 and 1.2 m between the beginning (point 1) and the end of the recharge period (point 3) decreases by 2.5×10^2 Pa. This decrease implies that some liquid water is replaced by steam. Assuming that initially the conduit had only liquid water with a density of ~970 kg/m^3, by the end of recharge the density decrease is ~80 kg/m^3. This value would arise if ~8 vol.% of the liquid is replaced by vapor, equivalent to a steam mass fraction of $\sim 5 \times 10^{-5}$.

We observe a water pressure signal with a period of 1 to 2 s during a geyser cycle (Fig. 12). One possible source of such periodic signals is resonance within the geyser conduit. Periodic signals were documented at other geysers (e.g. Kieffer, 1984; Lu and Kieffer, 2009) and seismic tremor is widely documented at magmatic volcanoes (e.g., Chouet, 1992; Johnson and Ripepe, 2011; Denlinger and Moran, 2014).

Resonance and damping of the perturbations are controlled by the geometry of the conduit, and the sound speed in the fluid U. In a pipe closed at one end, resonant frequencies f of a water column with height Z are (e.g., Kinsler et al., 1982)

$$f = \frac{nU}{4Z}, \tag{21}$$

where n is the mode (odd integer values, with $n = 1$ being the fundamental mode and higher values being overtones), and we assume U constant. The equilibrium sound speed of water + steam mixtures with a vapor mass fraction of 5×10^{-5} is $U \sim 1$ m/s (the non-equilibrium sound speed is >40 m/s; Karlstrom et al., 2013). The fundamental mode for a water column height of 0.85 m (approximate water level from the bottom of the conduit before eruption) is then ~3.4 s

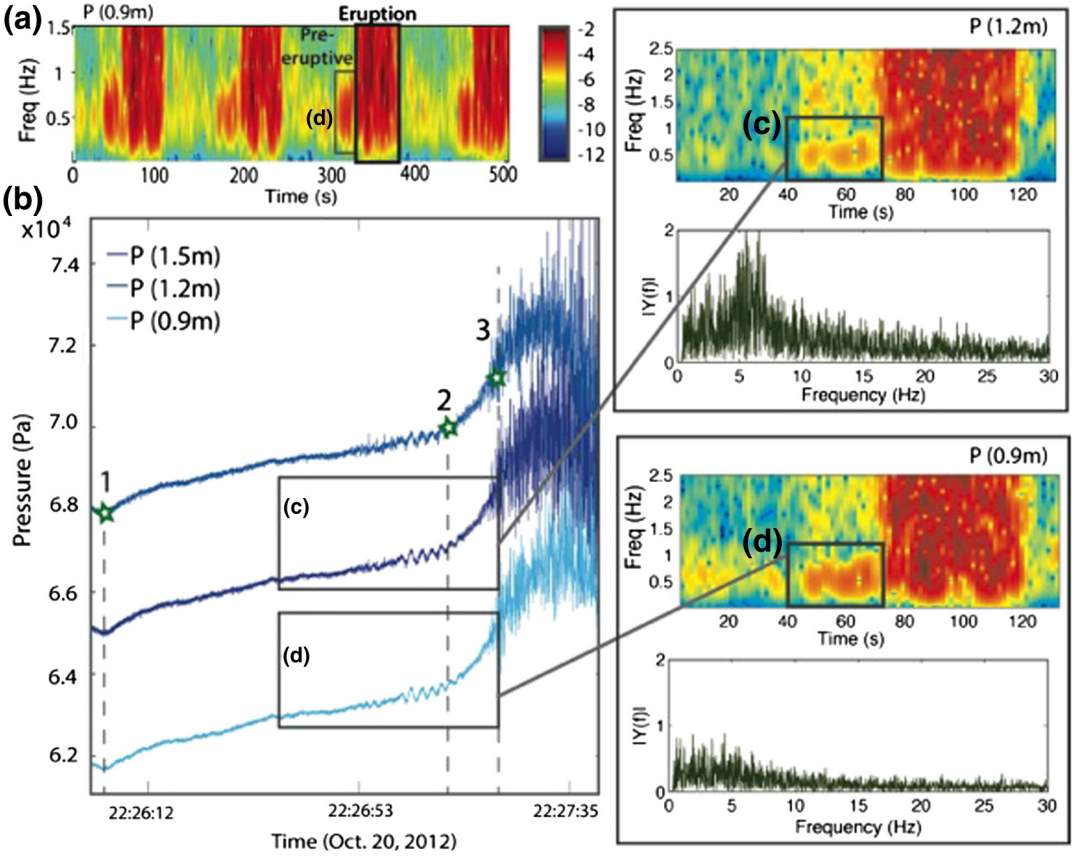

Fig. 12. (a) Spectrogram of four eruption cycles (pressure sensor at 1.5 m). We observe the same pre-eruption signal in every cycle. (b) Time series of pressure during the resting time and beginning of the eruption. Spectrograms of pressure at (c) 1.2 m, and (d) 0.9 m show that the main frequency in the pre-eruptive signal is 0.5 Hz. Plots below the spectrograms (dark green line) in (c) and (d) show the single-sided amplitude spectrum based on fast Fourier transform (FFT). (For interpretation of the references to color in this figure legend, the reader is referred to the web version of this article.)

(0.3 Hz). Our estimate is highly uncertain (the steam mass fraction is uncertain and is not likely to be uniform inside the conduit), and the value only differs by a factor of 2 to 3 from the 0.5 to 1 Hz signal that we see. We do not favor a resonance origin, however, because we do not see any overtones, nor any frequency gliding that might arise from temporal changes in steam mass fraction or water depth. Kedar et al. (1998) did not find evidence for conduit resonance at Old Faithful, Yellowstone either.

A second possible source of the oscillations is bubbles of steam or warm water entering the conduit from below every 1–2 s. Cross-correlation of the pressure measurements (Fig. 13) shows no time lag suggesting that all sensors are recording oscillations in the height of the water column. Several models of geysers describe "bubble traps" or cavities at depth, which are connected to the conduit and allow steam to accumulate and then be released into the geyser conduit (Mackenzie, 1811; Hutchinson et al., 1997; Belousov et al., 2013; Vandemeulebrouck et al., 2013; Adelstein et al., 2014). El Jefe's upper conduit ends at depth in a narrow crack, which may be connected to a similar bubble trap. A slug of steam passing through the crack can increase the water level in the conduit (Kedar et al., 1998). Increasing the elevation of the water column by injecting steam may explain the faster increase in pressure at the end of the recharge, ~10 s before the eruption (Fig. 11d). We visually observed a rapid increase of water level seconds before the eruption begins (down-hole video: electronic supplementary material).

5.3.3. Eruption

Water below the air–water interface is near boiling temperatures during the entire cycle. An additional input of heat into the system increases the water temperature, and a large mass of water boils in the upper conduit (Fig. 7c, points 3 to 4). Once the eruption begins, we see large pressure fluctuations, similar to those attributed by Kedar et al. (1998) to boiling and bubble collapse. The volume expansion of water when it boils will increase the pressure above the liquid surface and hence increase pressure at greater depths as well.

Once an explosive eruption begins at the surface, water is removed from the conduit (Figs. 5 and 7 points 3 to 6), and the fluid in the conduit decompresses (Fig. 8 points 4 to 6). Boiling conditions propagate downward (Fig. 8 points 5 to 6). By the time the system at depth reaches the maximum temperature, the eruption of water ends at the surface

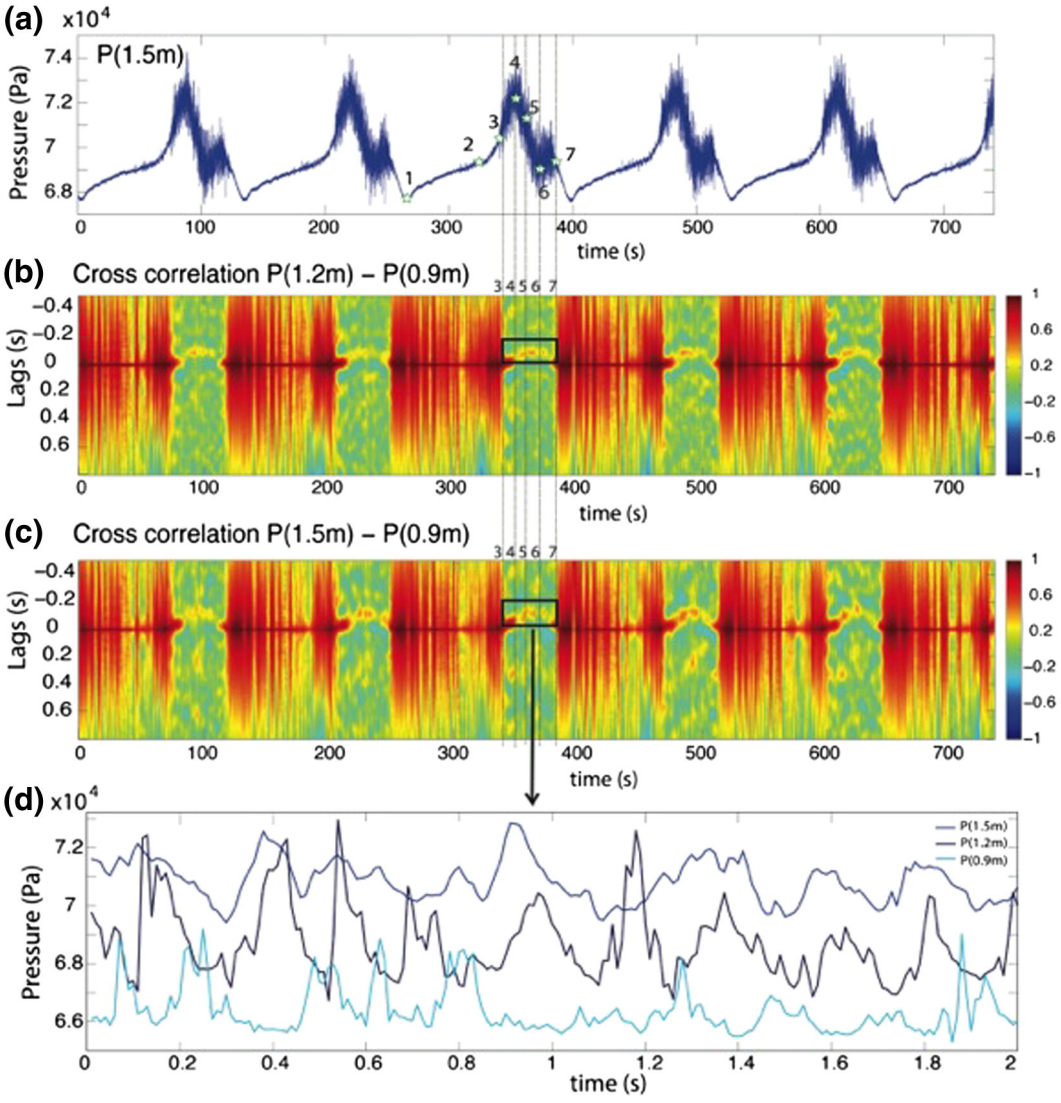

Fig. 13. (a) Pressure data of a subsample of five eruptions from a sensor located at a depth of 1.5 m. Plots (b) and (c) show the cross-correlation between pressure data from different depths. Time is shown on the horizontal axis and the vertical axis shows the time lag (in seconds) for the cross-correlation. (b) Cross-correlation of sensors located at 1.2 m and 0.9 m, showing a strong cross-correlation at a time lag of −0.1 s (black box). The negative lag means that the signal arrives first at 1.2 m and then at 0.9 m, propagating upward with a speed of 3 m/s. (c) Cross-correlation between sensors located at 1.5 m and 0.9 m, showing a strong signal at −0.15 s (black box). The pressure signal is moving upward with a speed of 4 m/s. (d) Pressure data subsample of 2 s during the eruption.

(Figs. 5 and 8, point 6). Temperature decreases at depth (Fig. 8 points 6 to 7), suggesting that heat is lost, however boiling continues in the upper part of the water column because pressure continues to decrease (points 6 to 7 in Figs. 7c and 8a). However, in the deeper part of the conduit (Fig. 8c) there is a slight increase of pressure that can be explained by lesser amounts of steam at depth. These observations suggest a non-uniform distribution of steam through the conduit. Water at depth stays below the boiling curve (Fig. 8, points 6 to 7c). Refilling by erupted water cools the conduit and ends the cycle (Fig. 7c, points 7 to 1).

Boiling conditions alone are not sufficient to cause an explosive eruption as boiling conditions persist after the eruption ends. The addition of steam from below the conduit, combined with a small enough volume of the cavity above the boiling surface, may be necessary to create pressures from boiling sufficient to initiate and sustain the eruption.

We performed a moving-window cross-correlation between pressure fluctuations recorded at different depths during the eruption. We find that pressure fluctuations propagate upward with a speed of 3 to 4 m/s (Fig. 13). This measured speed is the sum of the upward propagation velocity of pressure waves and upward velocity of the fluid in the conduit. Speeds of a few m/s would empty the conduit very rapidly, so we assume that at depth the propagation speed is close to 3–4 m/s. Using the model for the sound speed of liquid + steam mixtures under conditions of thermodynamic equilibrium (Kieffer, 1984; Lu and Kieffer, 2009), the implied steam mass fraction during the eruption is of the order of 1.2×10^{-3} ($U = 3$ m/s) to 1.7×10^{-3} ($U = 4$ m/s), using the formulation presented in Karlstrom et al. (2013); the equivalent volume fraction of steam is between 0.75 and 0.80 (using steam density of 0.4 kg/m^3 and liquid water density of 970 kg/m^3 for P_{air} and T_{boil}). These values suggest that the steam mass fraction during the eruption is two orders of magnitude higher than the amount of steam present in the conduit during recharge (inferred from the pressure changes described in the previous section).

The exit velocity v of the steam + liquid mixture can be estimated from the eruption height h by converting kinetic energy to potential energy, $v = \sqrt{2gh}$. The value of h varies during the eruption; using FLIR images and video recording we estimated the maximum $h < 2$ m (Fig. 5), thus $v < 6$ m/s. This value is higher than, but still close to, the sound speed inferred from propagating pressure signals, suggesting that the flow may in fact be choked to the equilibrium sound speed at the vent. However, uncertainties on the mass fraction of steam are too large to make this inference robust. Considering v and the size of the geyser mouth ($r \sim 0.15$ m), the exiting volume flux of liquid–steam mixture is 0.42 m^3/s, which is 3 orders of magnitude higher than discharge of liquid water measured at the surface.

During the eruption, the temperature at depth increases by ~3 °C (Fig. 7, points 3 to 4). We calculated the heat added to the system that is needed to increase the temperature of the column water by 3 °C. Considering an average mass of the erupted water of >110 kg, we obtain ~1.4×10^6 kJ, using $H_{erupted} = C_p mT$, and $C_p = 4.2$ kJ/kg °C. The amount of vapor condensation needed to heat this water is ~0.52 kg, using a latent heat of 2660 kJ/kg (for P_{air} and T_{boil}). The implied volume of steam required is ~1.24 m^3 (steam density 0.4 kg/m^3), equivalent to a cavity ~1 m in diameter. ~0.52 kg of steam in 110 kg of water is equivalent to a steam mass fraction of 4.7×10^{-3}, consistent with the previous estimates given the large uncertainty associated with the inferred sound speed (again, using the equilibrium sound speed).

The tilt data are noisy and likely influenced by the ponding and flow of water at the surface. However, when the tilt data are stacked, we do see a correlation with pressure in the conduit (Fig. 6ab). At El Jefe we see deformation, as recorded by the tilt that tracks the pressure in the conduit. Large increases of the tilt occur at the beginning of the eruption. In contrast, previous studies of geysering wells documented rapid decrease of the tilt during the eruption and gradual recovery during the quiescent period associated with recharge of water (Nishimura et al., 2006; Rudolph et al., 2012). The nature of the conduit may explain the difference: the previous studies were conducted at the Onikobe geyser, Japan and Old Faithful Geyser of Calistoga, California, which are artificial geysers whose conduits are metal pipes that isolate processes within the conduit from ground deformation.

5.3.4. Relaxation

At the end of the eruption, the large amplitude pressure fluctuations end. Boiling ends, and colder erupted water enters the conduit. Pressure and temperature smoothly decrease until the cycle starts again.

5.3.5. Conceptual model

Fig. 14 illustrates the conceptual model for all the key stages in the geyser cycle:

(1) Recharge: A single reservoir dominates recharge to the conduit. The pressure P_∞ in the reservoir is constant, and exceeds the pressure inside the conduit $P(t)$. The temperature of the reservoir is constant, T_∞. The filling process is adiabatic, and reaches boiling conditions at the top of the water column $T(t) \sim T_{boil}$. The rate of recharge $G(t)$ and pressure increase $P(t)$ inside the conduit decrease over time. Pressure in the conduit is close to hydrostatic and depends on the water level.

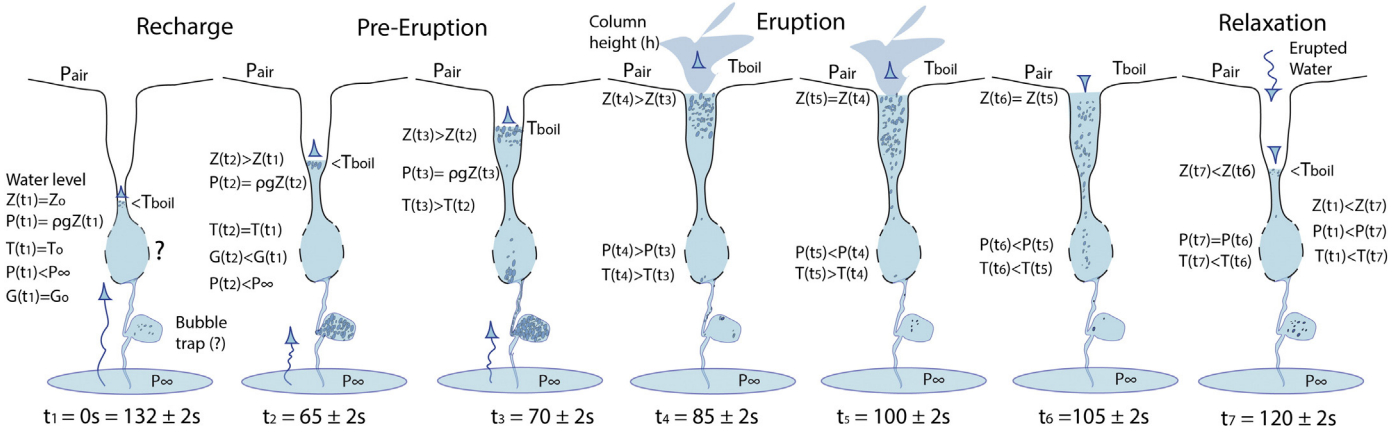

Fig. 14. Conceptual model for El Jefe geyser showing the different stages of the eruption cycle: recharge, pre-eruption, eruption, and relaxation. The model includes a bubble trap or cavity adding steam to the conduit. Blue dots inside the conduit represent bubbles of steam. Blue background represents liquid water. Conditions of pressure (P), temperature (T), water level (Z), and mass flow (G) inside the conduit evolve with time. The progression from t1 to t7 corresponds to the key stages in the cycle (Fig. 3). (For interpretation of the references to color in this figure legend, the reader is referred to the web version of this article.)

(2) Pre-eruptive stage: At the end of the recharge, steam bubbles from below (bubble trap) add latent heat to the system. $P(t)$ and $T(t)$ increase rapidly, and initiate explosive boiling at the top of the conduit.
(3) Eruption: During the eruption there is explosive discharge of water at the surface driven by rapid expansion of steam. The eruption column increases in height. Boiling conditions propagate downward in the conduit, as pressure decreases and temperature reaches a maximum value. The eruption at the surface ends but the column of water in the conduit is still at boiling conditions. Cooler erupted water enters the conduit, cooling the top of the water column (Fig. 7c). Large amplitude pressure fluctuations are caused by some combination of boiling, cavitation, and bursting of steam bubbles at the liquid surface.
(4) Relaxation: Once the eruption stops, temperature and pressure inside the conduit continue decreasing, remaining close to the boiling curve until initial conditions are restored.

6. Conclusions

Our work at El Jefe geyser provides a unique dataset, with a complete record of pressure and temperature inside a geyser conduit during complete geyser cycles over a large number of eruptions. We document the different stages of the geyser cycle, we calculate the fluid properties during an eruption, and we infer thermodynamic conditions at depth. Rapid boiling of a large mass of water occurs at the top of the water column. Water is then removed from the conduit and the remaining water decompresses, causing the boiling front to propagate downward. Eruption terminates when the addition of steam has ceased.

In the introduction we highlighted a few outstanding questions that our measurements allow us to address:

(1) How is heat transported? Steam ascending from depth provides thermal energy used in boiling during the eruption at El Jefe geyser. A small mass fraction of steam (order of $\sim 10^{-3}$) is enough to produce an eruption. We infer sound speeds for liquid + steam mixtures between 3 and 5 m/s. There is a possibility that flow may be choked at the vent, but uncertainties are too large to be conclusive.
(2) What is the geometry of the subsurface and its role? The dynamics of the eruptions are dominated by geometrical and thermodynamic complexities in the conduit and reservoir system below the near-surface conduit, allowing the accumulation and periodic release of steam in a reservoir that acts as a "bubble trap".
(3) How do geysers respond to external influences? Data do not show modulation of the interval between eruption (IBE) by external perturbations, implying an internal control on the geyser cycle. It also suggests that the thermal reservoir is very large relative to the amount of water erupted for this geyser.

El Jefe geyser had an extremely regular eruptive cycle at least during the week it was monitored, which contradicts the long-standing legend that the El Tatio geysers erupt when the sun rises.

Acknowledgments

This research was supported by the National Science Foundation (EAR1114184), and CEGA, University of Chile. We thank El Tatio team members who provided essential help in the laboratory and in the field: Fred Murphy, Ameeta Patel, Angello Negri, Pablo Ortega, Alberto Ardid, Cyndi Kelly, and Sarah Barrett. Eric King built the video camera system and took videos in the field. The fieldwork was performed with the permission of the Amayras Communities of Caspana and Toconce. We also thank Professor Lionel Wilson, Editor of Journal of Volcanology and Geothermal Research, the reviewers Dr. Atsushi Toramaru, Dr. Alexander Belousov, Fred Murphy, internal reviewer for USGS, and Jenny Baca for first edition. Any use of trade, firm, or product names is for descriptive purposes only and does not imply endorsement by the U.S. Government.

Appendix A. Supplementary data

Supplementary data to this article can be found online at http://dx.doi.org/10.1016/j.jvolgeores.2015.01.002.

References

Adelstein, E., Tran, A., Muñoz-Saez, C., Shteinberg, A., Manga, M., 2014. Geyser preplay and eruption in a laboratory model with a bubble trap. J. Volcanol. Geotherm. Res. 285, 129–135. http://dx.doi.org/10.1016/j.jvolgeores.2014.08.005.
Agnew, D.C., 2012. SPOTL: Some Programs for Ocean-Tide Loading.
Allen, E., Day, A., 1935. Hot springs of the Yellowstone National Park. Carnegie Inst. Wash. Publ. 466, 525.
Belousov, A., Belousova, M., Nechayev, A., 2013. Video observations inside conduits of erupting geysers in Kamchatka, Russia, and their geological framework: implications for the geyser mechanism. Geology 41, 387–390. http://dx.doi.org/10.1130/G33366.1.
Birch, F., Kennedy, G.C., 1972. Note on geyser temperatures in Iceland and Yellowstone National Park. In: Heard, H.C., Borg, I.Y., Rayleigh, C.B. (Eds.), Flow and Fracture of Rocks. American Geophysical Union Geophysical Monograph Series 16, pp. 329–336.
Bloss, F.D., Barth, T.F.W., 1949. Observations on some Yellowstone geysers. Geol. Soc. Am. Bull. 60, 861–886.
Bryan, T.S., 1995. The Geysers of Yellowstone. Univ. Press of Colorado, Boulder, Colorado (463 pp.).
Bunsen, R.W., 1847. Physikalische Beobachtungen uber die hauptsachlichsten Geysir Islands. Ann. Phys. Chem. 83, 159–170.
Chouet, B., 1992. A seismic model for the source of long-period events and harmonic tremor. Volcanic seismology. Springer, Berlin Heidelberg, pp. 133–156.
Cortecci, G., Boschetti, T., Mussi, M., Lameli, C.H., Mucchino, C., Barbieri, M., 2005. New chemical and original isotopic data on waters from El Tatio geothermal field, northern Chile. Geochem. J. 39 (6), 547–571.
Cusicanqui, H., Mahon, W.A.J., Ellis, A.J., 1975. The geochemistry of the El Tatio geothermal field, Northern Chile. Second United Nations Symposium on the Development and Utilization of Geothermal Resources, pp. 703–711 (San Francisco).
Cusicanqui, H., Mahon, W.A.J., Ellis, A.J., 1976. The geochemistry of the El Tatio geothermal field, northern Chile. Proc. 2nd U.N. Symposium on Geothermal Fields, Berkeley, California, pp. 140–156.
Denlinger, R.P., Moran, S.C., 2014. Volcanic tremor masks its seismogenic source: results from a study of noneruptive tremor recorded at Mount St. Helens, Washington. J. Geophys. Res. Solid Earth 119 (3), 2230–2251.
Fernandez-Turiel, J.L., Garcia-Valles, M., Gimeno-Torrente, D., Saavedra-Alonso, J., Martinez-Manent, S., 2005. The hot spring and geyser sinters of El Tatio, Northern Chile. Sediment. Geol. 180 (3), 125–147.
Fournier, R.O., 1969. Old faithful: a physical model. Science 163, 304–305.
Fukutomi, T.A., 1942a. New mechanism of the geyser I. Bull. Seism. Soc. Jpn. 14, 157–174.
Fukutomi, T.A., 1942b. New mechanism of the geyser II. Bull. Seism. Soc. Jpn. 14, 189–202.
Giggenbach, W.F., 1978. The isotopic composition of waters from the El Tatio geothermal field, Northern Chile. Geochim. Cosmochim. Acta 42, 979–988.
Glennon, J.A., Pfaff, R.M., 2003. The extraordinary thermal activity of El Tatio Geyser Field, Antofagasta Region, Chile. GOSA Trans. 8, 31–78.
Healy, J., 1974. Geological report on El Tatio geothermal field, Antofagasta province, Chile. UNDP-Report.
Hurwitz, S., Kumar, A., Taylor, R., Heasler, H., 2008. Climate-induced variations of geyser periodicity in Yellowstone National Park, USA. Geology 36, 451–454.
Hurwitz, S., Hunt, A.G., Evans, W.C., 2012. Temporal variations of geyser water chemistry in the Upper Geyser Basin, Yellowstone National Park, USA. Geochem. Geophys. Geosyst. 13, Q12005. http://dx.doi.org/10.1029/2012GC004388.
Hurwitz, S., Sohn, R.A., Luttrell, K., Manga, M., 2014. Triggering and modulation of geyser eruptions in Yellowstone National Park by earthquakes, earth tides, and weather. J. Geophys. Res. 119, 1718–1737. http://dx.doi.org/10.1002/2013JB010803.
Husen, S., Wiemer, S., Smith, R.B., 2004a. Remotely triggered seismicity in the Yellowstone National Park region by the 2002 Mw 7.9 Denali Fault earthquake, Alaska. Bull. Seismol. Soc. Am. 94, S317–S331.
Husen, et al., 2004b. Changes in geyser eruption behavior and remotely triggered seismicity in Yellowstone National Park produced by the 2002 M 7.9 Denali Fault earthquake, Alaska. Geology 32, 537–540. http://dx.doi.org/10.1130/G20381.
Hutchinson, R.A., 1985. Hydrothermal changes in the upper Geyser Basin, Yellowstone National Park, after the 1983 Borah Peak, Idaho, earthquake. In: Stein, R.S., Bucknam, R.C. (Eds.), Proceedings of Workshop 28—On the Borah Peak, Idaho, earthquake: U.S. Geological Survey Open-File Report OF 85-0290-A, pp. 612–624.
Hutchinson, R.A., Westphal, J.A., Kieffer, S.W., 1997. In situ observations of Old Faithful Geyser. Geology 25, 875–878.
Ingebritsen, S.E., Rojstaczer, S.A., 1993. Controls on geyser periodicity. Science 262, 889–892. http://dx.doi.org/10.1126/science.262.5135.889.
Ingebritsen, S.E., Rojstaczer, S.A., 1996. Geyser periodicity and the response of geysers to deformation. J. Geophys. Res. 101, 21,891–21,905. http://dx.doi.org/10.1029/96JB02285.

Johnson, J.B., Ripepe, M., 2011. Volcano infrasound: a review. J. Volcanol. Geotherm. Res. 206 (3), 61–69.
Karlstrom, L., Hurwitz, S., Sohn, R.A., Vandemeulebrouck, J., Murphy, F., Rudolph, M.L., Johnston, M.J.S., Manga, M., McCleskey, R.B., 2013. Eruptions at Lone Star Geyser, Yellowstone National Park, USA, Part 1: energetics and eruption dynamics. J. Geophys. Res. Solid Earth 118, 1–15. http://dx.doi.org/10.1002/jgrb.50251.
Kedar, S., Kanamori, H., Sturtevant, B., 1998. Bubble collapse as the source of harmonic tremor at Old Faithful Geyser. J. Geophys. Res. 103, 24,283–224,299. http://dx.doi.org/10.1029/98JB01824.
Kieffer, S.W., 1984. Seismicity at Old Faithful Geyser: an isolated source of geothermal noise and possible analogue of volcanic seismicity. J. Volcanol. Geotherm. Res. 22, 59–95.
Kieffer, S.W., 1989. Geologic nozzles. Rev. Geophys. 27, 3–38. http://dx.doi.org/10.1029/RG027i001p00003.
Kinsler, L.E., Frey, A.R., Coppens, A.B., Sanders, J.V., 1982. Fundamentals of Acoustics. 3rd edition. Wiley, New York.
Kiryukhin, A.V., Rychkova, T.V., Dubrovskaya, I.K., 2012. Formation of the Hydrothermal System in Geysers Valley (Kronotsky Nature Reserve, Kamchatka) and Triggers of the Giant Landslide. Appl. Geochem. 27, 1753–1766. http://dx.doi.org/10.1016/j.apgeochem.2012.02.011.
Lahsen, A., 1976a. La actividad geotermal y sus relaciones con la tectónica y el volcanismo en el norte de Chile. I Congreso Geológico Chileno, Actas. Antofagasta, pp. B105–B127.
Lahsen, A., 1976b. Geothermal exploration in Northern Chile. Proceedings of the Circum Pacific Energy and Mineral Resources Conference, Honolulu Memoir 25, pp. 169–175.
Lahsen, A., Trujillo, P., 1975. El Tatio geothermal field. Proceedings of the Second United Nations Symposium on the Development and Use of Geothermal Resources, San Francisco, CA, Memoir 1, pp. 157–178.
Lahsen, A., Trujillo, P., 1976. El campo geotermico de El Tatio, Chile. Proyecto Geotermico CORFO-ONU. Internal Report.
Landrum, J.T., Bennett, P.C., Engel, A.S., Alsina, M.A., Pastén, P.A., Milliken, K., 2009. Partitioning geochemistry of arsenic and antimony, El Tatio Geyser Field, Chile. Appl. Geochem. 24, 664–676.
Lu, X., Kieffer, S.W., 2009. Thermodynamics and mass transport in multicomponent multiphase H_2O systems of planetary interest. Ann. Rev. Earth Planet. Sci. 37, 449–477.
Mackenzie, G., 1811. Travels in the Island of Iceland, Edinburgh vol. 27. Alam and Company, Edinburgh.
Manga, M., Brodsky, E.E., 2006. Seismic triggering of eruptions in the far field: volcanoes and geysers. Ann. Rev. Earth Planet. Sci. 34, 263–291.
Marler, G.D., 1951. Exchange of function as a cause of geyser irregularity [Wyoming]. Am. J. Sci. 249, 329–342. http://dx.doi.org/10.2475/ajs.249.5.329.
Marler, G.D., 1964. Effects of the Hebgen Lake earthquake of August 17, 1959 on the hot springs of the Firehole geyser basins, Yellowstone National Park. U.S. Geol. Surv. Prof. Pap. 435, 185.
Marler, G.D., White, D.E., 1975. Seismic geyser and its bearing on the origin and evolution of geysers and hot springs of Yellowstone National Park. Geol. Soc. Am. Bull. 86, 749–759.
Merzhanov, A.G., Shteinberg, A.S., Shteinberg, G.S., 1990. Heat and mass exchange in geyser systems. In: Hestroni, G. (Ed.), Proceedings of the 9th International Heat Transfer Conference, pp. 323–328.
Munoz, M., Hamza, V., 1993. Heat cihttp:dients in Chile. Stud. Geophys. Geod. 37, 315–348. http://dx.doi.org/10.1007/BF01624604.
Namiki, A., Munoz-Saez, C., Manga, M., 2014. El Cobreloa: a geyser with two distinct eruption styles. J. Geophys. Res. 119. http://dx.doi.org/10.1002/2014JB11009.
Nicolau, C., Reich, M., Lynne, B., 2014. Physico-chemical and environmental controls on siliceous sinter formation at the high-altitude El Tatio geothermal field, Chile. J. Volcanol. Geotherm. Res. 282, 60–76. http://dx.doi.org/10.1016/j.jvolgeores.2014.06.012.
Nishimura, T., Ichihara, M., Ueki, S., 2006. Investigation of the Onikobe geyser, NE Japan, by observing the ground tilt and flow parameters. Earth Planets Space 58, e21–e24.
Rinehart, J.S., 1972. Fluctuations in geyser activity caused by variations in Earth tidal forces, barometric pressure, and tectonic stresses. J. Geophys. Res. 77, 342–350. http://dx.doi.org/10.1029/JB077i002p00342.
Rinehart, J.S., 1980. Geysers and Geothermal Energy. Springer-Verlag, New York.
Rinehart, J.S., Murphy, A., 1969. Observations on pre- and post-earthquake performance of Old Faithful geyser. J. Geophys. Res. 74, 574–575.
Rojstaczer, S., Galloway, D.L., Ingebritsen, S.E., Rubin, D.M., 2003. Variability in geyser eruptive timing and its causes; Yellowstone National Park. Geophys. Res. Lett. 30 (18), 1953. http://dx.doi.org/10.1029/2003GL017853.
Rudolph, M.L., Manga, M., Hurwitz, S., Johnston, M.J., Karlstrom, L., Wang, C.-Y., 2012. Mechanics of old faithful Geyser, Calistoga, California. Geophys. Res. Lett. 39, L24308. http://dx.doi.org/10.1029/2012GL054012.
Shteinberg, A.S., 1999. An experimental study of geyser eruption periodicity. Power Eng. 366, 47–50.
Shteinberg, A., Manga, M., Korolev, E., 2013. Measuring pressure in the source region for geysers, Geyser Valley, Kamchatka. J. Volcanol. Geotherm. Res. 264, 12–16.
Steinberg, G.S., Merzhanov, A.G., Steinberg, A.S., 1982. Geyser process: its theory, modeling and field experiment. Part 4. On seismic influence on geyser regime. Mod. Geol. 8, 79–86.
Tassi, F., Martinez, C., Vaselli, O., Capaccioni, B., Viramonte, J., 2005. Light hydrocarbons as redox and temperature indicators in the geothermal field of El Tatio (northern Chile). Appl. Geochem. 20, 2049–2062.
Tassi, F., Aguilera, F., Darrah, T., Vaselli, O., Capaccioni, B., Poreda, R.J., Delgado Huertas, A., 2010. Fluid geochemistry of hydrothermal systems in the Arica-Parinacota, Tarapacá and Antofagasta regions (northern Chile). J. Volcanol. Geotherm. Res. 192, 1–15.
Vandemeulebrouck, J., Roux, P., Cros, E., 2013. The plumbing of Old Faithful Geyser revealed by hydrothermal tremor. Geophys. Res. Lett. 40, 1989–1993. http://dx.doi.org/10.1002/grl.50422.
Vandemeulebrouck, J., Sohn, R., Rudolph, M., Hurwitz, S., Manga, M., Johnston, M., Soule, A., McPhee, D., Glen, J., Karlstrom, L., Murphy, F., 2014. Eruptions at Lone Star geyser, Yellowstone National Park, USA: 2. Constraints on subsurface dynamics. J. Geophys. Res. Solid Earth 119. http://dx.doi.org/10.1002/2014JB011526.
White, D.E., 1967. Some principles of geyser activity, mainly from Steamboat Springs, Nevada. Am. J. Sci. 265, 641–684.
White, D.E., Marler, G.D., 1972. Fluctuations in geyser activity caused by Earth tidal forces, barometric pressure, and tectonic stresses. Comment. J. Geophys. Res. 77, 5825–5829. http://dx.doi.org/10.1029/JB077i029p05825.

Online References

Omega Thermocouple Home Page. Thermocouple Probes. N.p., n.d. Web. 09 Aug. 2014. http://www.omega.com/thermocouples.html.
Webbook Thermophysical Properties of Fluid Systems. N.p., n.d. Web. 07 Aug. 2014. http://webbook.nist.gov/chemistry/fluid/.